MEMS DESIGN AND MODELLING BASED ON RESONANT GATE TRANSISTOR FOR COCHLEAR BIOMIMETICAL APPLICATION

Link:
Link to publication record in Edinburgh Research Explorer

Document Version:
Peer reviewed version

Published In:
Microsystem Technologies

MEMS DESIGN AND MODELLING BASED ON RESONANT GATE TRANSISTOR FOR COCHLEAR BIOMIMETICAL APPLICATION

R Latif[1,2,3], B. Y. Majlis[3] and R Cheung[1,2]
[1] Scottish Microelectronics Centre, [2]Institute for Integrated Micro and Nano Systems, The University of Edinburgh, King's Buildings, Edinburgh EH9 3JF, United Kingdom
[3]Institute of Microengineering and Nanoelectronics (IMEN), The National University of Malaysia, 43600 Bangi, Selangor, Malaysia
rhonira@ukm.edu.my

Abstract

The electromechanical behaviour and frequency response of the human cochlear have been described to be mimicked using an array of resonant gate transistors (RGT). Presented in this paper are the mathematical model, geometrical analysis and novel design of RGT, employed for the physical model development of the cochlea. In an array of RGTs, the aluminium bridge gate structures with length of 0.57 mm – 1.62 mm transduce the sound input signal into mechanical vibrations at audible frequency range of 1 kHz - 8 kHz. The channels underneath the bridge gates transduce the mechanical vibrations into small signal drain currents with reasonable estimated sensitivity of 4 nA/Pa - 17 nA/Pa. The gain amplification and resonant frequency reduction of RGT with respect to the voltage applied onto the bridge gate structure highlight the adaptive characteristics of a human cochlear. The proposed modelling approach can aid the fabrication design of RGT for cochlear model.

1   Introduction

The biological system with its exceptional capabilities has inspired many researchers to develop an artificial system that can mimic its natural behaviours. For examples, the jellyfish-inspired microrobots are created for underwater monitoring and exploration (Liwei et al. 2010) and the developed ultrathin porous nanocrystalline silicon dialysis membrane that can possibly be used in implantable artificial kidney (Striemer et al. 2007). The poured efforts on replicating the nature's complex mechanism are motivated by the aspirations to enhance human wellbeing, to solve engineering problems, to initiate advanced sensors of various kinds and to aid in understanding the biological mechanism. Our research focuses on the physical model development of a human cochlear using the microelectromechanical systems (MEMS) device called resonant gate transistor (RGT).

The audible frequency that can be perceived by a healthy human ear ranges between 20 Hz to 20 kHz with the intensity range above the threshold of hearing (0 dB) up until the threshold of pain (120 dB) (Moore 1997; Pickles 1988). The cochlea has a remarkable fast reaction up to 20 kHz as compared to the slower elbow muscle fibres contraction mechanisme (Latif et al. 2008). The sound input signals stimulate transverse vibrations with resonance amplitudes along the basilar membrane (BM) length in cochlea as illustrated in Fig. 1. The membrane possesses a tonotopic organisation characteristic that provides resonant frequency variation from 20 kHz at the basal end to 20 Hz at the apex of the membrane. Thus, each point on the membrane corresponds to different resonant frequency, making the whole basilar membrane structure to function as a real-time mechanical bandpass filter (White and Grosh 2005). Subsequently, the hair cells that sit on BM transduce the occurred mechanical vibrations into electrical signals. The induced AC electrical signals within the hair cells follow the sound input stimulation waveform, like a microphone. The frequency response of one hair cell has been

reported to possess the broadly-tuned electrical bandpass characteristic that follows closely the mechanical response of a section point in the membrane (Moore 1997; Pickles 1988).

The active cochlea amplification has been predicted and eventually measured decades ago, with electromechanical basis consideration of the structure. However, the actual mechanism involved that can describe the active cochlea behaviour is unknown and has since become a fundamental scientific interest for many researchers. The physical models and theories on cochlea motion amplification have been developed and many have postulated that it is either 1) the hair cell that increased the BM motion, 2) the hair cell that increased its own sensitivity or 3) both (Bell 2006; Elliott and Shera 2012; Robles and Ruggero 2001). The cochlea motion is amplified at low sound pressure level while at higher sound pressure level, the gain is reduced to compress the dynamic range.
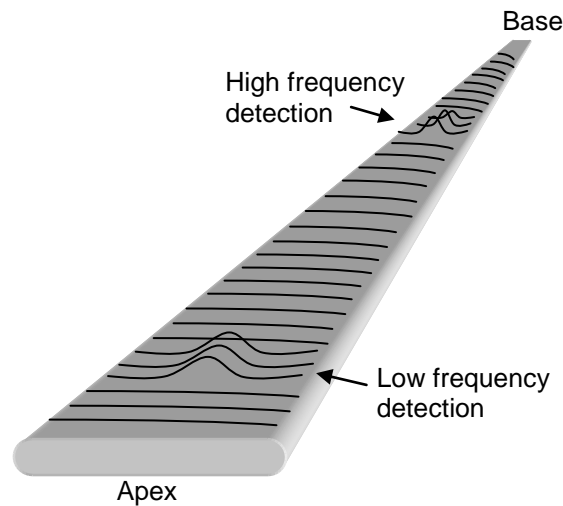

Fig. 1 The schematic diagram of a basilar membrane in an uncoiled cochlea that generates a tonotopic mapping of frequency along its length. The membrane peaks at different places for different excitation frequencies, providing a tonotopic distribution of frequency. High frequencies are detected close to the base section while low frequencies at the apex partition of the basilar membrane

The fact that the cochlea itself is an electromechanical acoustic transducer and the advanced development of micro- and nanofabrication technology have drawn researchers' attention to employ MEMS in cochlear model (Bachman et al. 2006; Haronian and MacDonald 1995). An array of MEMS resonators for examples the cantilevers and bridges, each with a specific resonant frequency can perform the passive parallel spectral filtering in a similar manner with the BM. Haronian and MacDonald (1995) have demonstrated that a large array of silicon bridges with exponentially varying length possessed similar mechanical behaviour as the cochlea. Small spacing distance between the bridges caused the bridges to be coupled by the viscosity of air, mimicking the cochlea's travelling wave phenomenon. An array of polymer cantilevers with different length has been fabricated by Bachman et al. (2006) to mimic the response of human cochlear. The cantilevers filtered the sound frequency mechanically in parallel with low latency in the output signal. The developed device can be integrated with electronic circuitry, suggesting for a completely implantable bionic ear. Liu (2007) has reported on biomimetic artificial hair cell sensors using micromachined cantilever with a vertical hairlike vibrating structure attached at the free end. Not many researchers however have successfully transduced the mechanically filtered sound into electrical signals, mimicking the hair cells' function in human.

In our work, the mechanical vibration and spatial arrangement of frequency along the basilar membrane length in cochlea are proposed to be simulated by the bridge gates of the RGTs as shown in Fig. 2. Concurrently, the electrical signals within the hair cells of the cochlea can be reproduced by the channel region between the source and drain of RGT. The fabrication process, measurement analysis and interface circuit design for RGT can be found in (Koickal et al. 2011; Latif 2012; Latif et al. 2010; Latif et al. 2011; Mastropaolo et al. 2013;

Mastropaolo et al. 2012; Wang et al. 2012). In this paper, the mathematical model of RGT device employed in cochlear model has been developed. The formulated equations can be used to assist the fabrication design of RGT cochlear model. The mathematical model of RGT cochlear model has been simplified by incorporating the lumped element model of the bridge gate, the modified transistor equation of the channel and the electromechanical mechanism of the bridge gate.
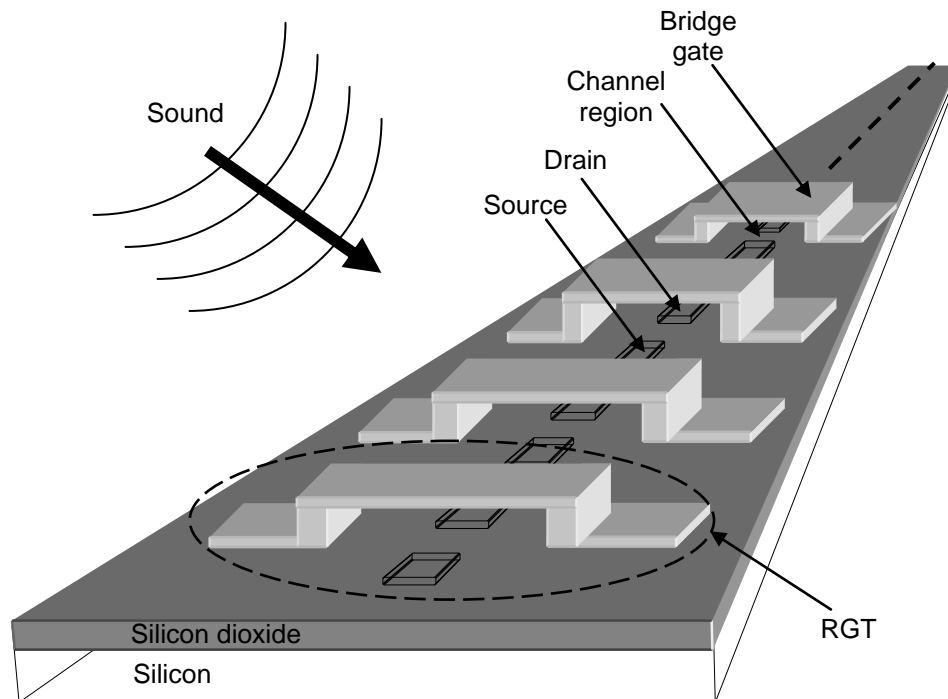

Fig. 2 The schematic diagram of RGT cochlear model. The basic building block for the RGT consists of the mechanical bridge gate structure and the electrical channel region between source/drain. An array of RGTs is employed in the RGT cochlear model in order to obtain the multichannel filtering of the sound input signals. The RGTs mimic the electromechanical response of a cochlea that detects sound as mechanical vibrations and then transformed into electrical signals

2   Structure and principle of operation

Nathanson et al have first reported on the fabrication of RGTs that operate within the frequency range of 2.8 kHz - 60 kHz (Nathanson and Newell 1965; Nathanson et al. 1967). The devices were actuated electrostatically by the AC signals and employed as low frequency monolithic audio oscillators. In our study, the operation of RGT has been analysed based on the mechanical sound pressure wave input signals in order to apply the device into the cochlear model. In Fig. 2, the sound pressure waves actuate mechanically the RGT devices. The bridge gate of RGT acts as a vibration transducer, transforming the sound pressure wave input signals into mechanical vibrations with a certain value of quality factor, resonant frequency and displacement. The vibration pattern of the bridge gate array embodies the information regarding the frequency, amplitude and time of the sound input signals.

In this paper, the bridge gate is modelled using discrete lumped element model system and the calculated output is compared with the finite element model. The geometrical dimensions of the bridge gate can be manipulated in order to attain certain values of resonant frequency and quality factor. Basically, the sensitivity and frequency selectivity of bridge gate can be designed from its geometry, material properties and the medium viscosity that surrounds the bridge gate (Bachman et al. 2006; Haronian and MacDonald 1995; White and Grosh 2002). An array of RGTs with different length of bridge gates, each can responds to different resonant frequency f_1, imitating the spatial arrangement of frequency along the basilar membrane length in cochlea. The bridge gates

are biased with DC voltages in order to transduce the mechanical vibrations into electrical signals within the channels. The sensitivity of the bridge structure could be tuned simply by varying the applied DC bias voltage. The ability to perform self-controlled gain from each individual bridge gate structure imitates the adaptive characteristics of the cochlea.

The channel region with source/drain of RGT is located underneath the bridge gate. The applied DC voltage onto the bridge gate induces charges within the channel and modulates the channel conductance. A DC bias voltage is also applied between the source and drain that allows the electrical current signal to flow through the channel. The bridge gate mechanical vibrations are then transformed into electrical current signal that flows from drain to source. Basically, the bridge gate of RGT acts like a gate for the underneath channel region as in the gate for metal-oxide-semiconductor field-effect transistor (MOSFET) device. Without the channel, the mechanical vibrations of the bridge structure can be detected capacitively. Compared to the capacitive detection method, a channel-based detection technique might propose signal amplification advantage and thus promises higher output capability (Abelé et al. 2005). The channel of RGT is modelled by including the effect of air gap into the standard transistor equations. It is known that the channel of MOSFET possesses transconductance which represents gain of the device. The transconductance magnitude can be designed from the dimensions of the channel region.

3 Bridge gate mechanical modelling and design.

In this section, the geometrical dimensions and material for the RGT bridge gate structure have been designed to mimic the response of a human cochlear. The equivalent lumped element model of the RGT bridge gate structure has been developed in order to estimate the mechanical sensitivity of the structure operating in air and compared with the numerical finite element model. The mechanical sensitivity of the bridge gate is defined as the change in vibration displacement with respect to the change of sound input pressure applied on the device structure. The mechanical response has been estimated with respect to constant load input pressure and noise input signals of 0.01 Pa.

3.1 Resonant frequency design for bridge gate

Ten RGT devices have been considered to cover the mechanical resonant frequency points, f_1 from 1 kHz to 8 kHz and the bridge gates are labelled as B1 until B10. Equ. (1) can be used to design an array of bridge gates that resonates within a certain frequency range where γ is 4.73 for fundamental mode vibration, $A_b = w_b t_b$ is the cross sectional area with w_b and t_b being the width and thickness of the bridge gate, E is the Young's modulus, $I = \frac{w_b t_b^3}{12}$ is the moment of inertia, ρ is the density and l_b is the length of the bridge gate structure (Han et al. 1999).

$$f_1 = \frac{\gamma^2}{2\pi} \sqrt{\frac{EI}{\rho A_b l_b^4}} \tag{1}$$

From Equ. (1), aluminium has been considered to be the material for the bridge gate structure, assuming $\rho = 2700$ kgm^{-3} and $E = 70$ GPa. In Table 1, the length of the aluminium bridge gates have been estimated to be $l_b = 1.62$ mm - 0.57 mm with $t_b = 0.5$ µm in order to achieve $f_1 = 1$ kHz - 8 kHz. The designed RGT array mimics the tonotopic organisation characteristic of the cochlea. The number of bridge gates can be increased to cover more frequency points as have been reported by White *et al* in which nearly 3000 suspended beams have been fabricated in order to deliver 3000 channels of frequency information (White and Grosh 2002).

Other than manipulating the bridge gate length and thickness, the resonant frequency f_1 of a bridge gate can be designed to operate within the audible frequency range by choosing the appropriate values of Young's modulus and density of the material structure. From Equ. (1), materials with relatively small $\frac{E}{\rho}$ ratio are desired in order to cover the audible frequency range signals. The usually available materials with small $\frac{E}{\rho}$ ratio are aluminium

4

($\frac{E}{\rho}$ ~ 26 MPa kg^{-1} m^3), tantalum ($\frac{E}{\rho}$ ~ 11 MPa kg^{-1} m^3), platinum ($\frac{E}{\rho}$ ~ 5 MPa kg^{-1} m^3) and copper ($\frac{E}{\rho}$ ~ 14 MPa kg^{-1} m^3), assuming bulk values of E and ρ for the metals. In Fig. 3, the resonant frequencies f_1 for the aluminium, tantalum, platinum and copper bridge gates of similar dimensions have been calculated and compared. Aluminium possesses relatively higher ratio of Young's modulus to density and therefore, a stress-free aluminium bridge gate structure will resonate at a higher resonant frequency compared to the ones calculated for the tantalum, platinum and copper bridge gates of the same length and thickness.

Table 1 The estimated aluminium bridge gate length l_b for the resonant frequencies of f_1 = 1 kHz - 8 kHz. An array of ten RGTs labelled as B1 - B10 has been designed to copy the spatial arrangement of frequency in the cochlea.

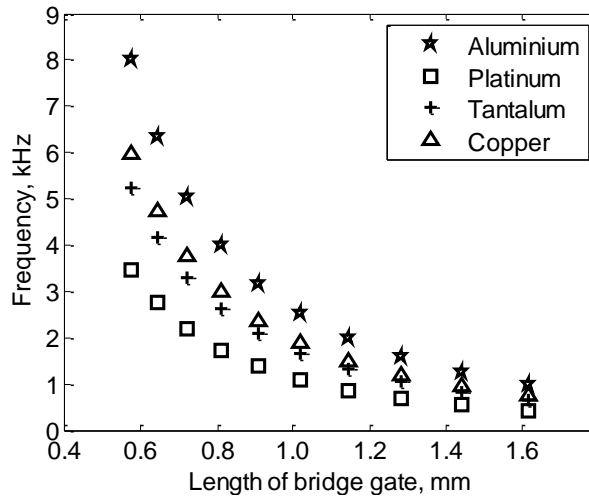| Label	f_1, kHz	l_b, mm
B10	8.0	0.57
B9	6.3	0.64
B8	5.0	0.72
B7	4.0	0.81
B6	3.2	0.91
B5	2.5	1.02
B4	2.0	1.14
B3	1.5	1.28
B2	1.3	1.44
B1	1.0	1.62

Fig. 3 The calculated resonant frequencies for platinum, tantalum, copper and aluminium bridge gates of length l_b = 1.62 mm - 0.57 mm and thickness t_b = 0.5 μm. The increase of $\frac{E}{\rho}$ ratio from platinum (5), tantalum (11), copper (14) to aluminium (26) increases the resonant frequency of the bridge gate structure

3.2 Mechanical equivalent lumped element model for bridge gate

The dynamic response of a bridge gate structure is analysed as a one-degree-of-freedom vibrating system in which the resonating structure is represented by a lumped mass, spring and damper. The general linear second order dynamic equation of the bridge gate is given by d'Alembert's principle in Equ. (2) where F is the net input force that induces sinusoidal deflection on the bridge gate, x is the instantaneous vibration displacement of the bridge gate with respect to time t, m represents the effective bridge gate mass which is approximately 0.767 times its actual mass when force F is distributed over the entire bridge gate, b is the damping coefficient of

bridge gate structure and k is the elastic restoring coefficient/the spring constant that quantifies the stiffness of bridge gate (Rebeiz 2003).

$$m\frac{\partial^2 x}{\partial t^2} + b\frac{\partial x}{\partial t} + kx = F \tag{2}$$

From Equ. (2), the amplitude and phase of the bridge gate vibrations are derived into the standard resonance equation in Laplace domain as given by Equ. (3) where ω_0 is the mechanical resonant radial frequency defined by Equ. (4) and Q_3 is the quality factor at 3 dB below the peak vibration defined by Equ. (5) with ζ as the damping ratio of the bridge gate structure (Rebeiz 2003).

$$\frac{X(s)}{F(s)} = \frac{1}{ms^2 + bs + k} = \frac{1}{k}\left[\frac{1}{1 + \left(\frac{s}{\omega_0}\right)^2 + \frac{s}{Q_3\omega_0}}\right] \tag{3}$$

$$\omega_0 = \sqrt{\frac{k}{m}} = 2\pi f_1 \tag{4}$$

$$Q_3 = \frac{k}{\omega_0 b} = \frac{1}{2\zeta} \tag{5}$$

3.2.1 Damping coefficient, b and quality factor, Q₃

The aluminium bridge gate can be designed to be at a certain distance d_i above the channel. Energy dissipation within the micromachined bridge gate structure can be described by several damping mechanisms that depend on d_i and air pressure conditions (Hall et al. 2008; Li and Fang 2009; Rebeiz 2003). Air can be used to dampen the oscillation of the vibrating bridge gates and the mechanism is known as the squeeze-film damping or air damping (Haronian and MacDonald 1995). For a MEMS resonating structure vibrating in standard atmospheric pressure and temperature, the squeeze-film damping will dominate, particularly when the gap size d_i between the structure and substrate is smaller compared to its width and length. The squeeze film damping b of the bridge gate and the corresponding quality factor approximation Q_3 can be calculated using Equ. (6) and Equ. (7) respectively, with ψ being the viscosity coefficient of the medium surrounding the bridge gate. At a very low pressure for example in vacuum medium, $\psi \rightarrow 0$ and the intrinsic material damping of the bridge gate will dominate over the squeeze film damping.

$$b = \frac{3}{2\pi}\frac{\psi(w_b l_b)^2}{d_i{}^3} \tag{6}$$

$$Q_3 = \frac{\sqrt{E\rho}t_b{}^2 d_i{}^3}{\psi\left(\frac{w_b l_b}{2}\right)^2} \tag{7}$$

The quality factor of each bridge gate is controlled by the damping of the structure through the pressure and viscosity of air, which exists between the bridge gates and between the bridge gate and substrate. The squeeze film damping between the bridge gates has not been studied here as isolated bridge gate analysis has been assumed. In our model, the damping of the bridge gate is presented by the damping ratio $\zeta = \frac{\omega_0 b}{2k} = \frac{1}{2Q_3}$. For model simplification at this stage, the bridge gates are assumed to be operating in standard atmospheric pressure with a constant damping ratio of $\zeta = 0.1$.

3.2.2 Spring constant, k

The stiffness of bridge gate for small deflection/vibration cases can be modelled using the linear spring constant, $k = k' + k''$ where k' accounts for the bridge gate material properties i.e. Young's modulus and moment of inertia while k'' quantifies the biaxial residual tensile stress induced within the bridge gate during the fabrication process. From the equation of bending, $k' = 32Ew_b \left(\frac{t_b}{l_b}\right)^3$ assuming uniform vertical force F is distributed across the entire bridge gate structure. As for the derivation of k'', the bridge gate is modelled as a stretched wire $k'' = 8\sigma_{tens}(1-v)w_b\left(\frac{t_b}{l_b}\right)$ with σ_{tens} being the biaxial residual tensile stress and v is the Poisson's ratio of the bridge gate (Rebeiz 2003). In the fabrication process, the biaxial residual compressive stress might be induced instead of tensile. For model simplification purpose, the bridge gates are assumed to be free of stress.

3.3 Mechanical response of bridge gate

The mechanical equivalent lumped element model for the aluminium bridge gates B1 - B10 from Table 1 have been created using the lumped element parameters m, b, and k. In the model, a constant bridge gate width of w_b = 10 μm has been considered for the bridge gate length of l_b = 1.62 mm - 0.57 mm. At this stage, the total damping is assumed to be constant for all bridge gate lengths. Later in the fabrication design section, the bridge gate width w_b needs to be varied for each bridge gate length in order to obtain constant damping.

The established lumped element model for the aluminium bridge gate B1 of length l_b = 1.62 mm has been tested by applying a uniform load of 0.01 Pa. The frequency response of B1 has been estimated from the analytical lumped element model and plotted in Fig. 4. In order to verify that the calculated analytical lumped element model for B1 is approximately adequate, the numerical finite element (FE) model of the aluminium bridge gate has been simulated using *CoventorWare*. The FE model for B1 has been constructed using similar geometrical dimensions and material properties. The steady state linear dynamic response of the constructed FE model for the bridge gate structure has been simulated with respect to the continuous harmonic excitation input of 0.01 Pa distributed over the entire structure. In Fig. 4, the FE simulation result for the aluminium bridge gate B1 is compared with the calculated response from the analytical lumped element model. The plot shows an excellent agreement between the two models with the expected resonant frequency of ~ 1 kHz, maximum displacement of ~ 1.25 μm and Q_{10} ~ 1. The value of Q_{10} refers to the quality factor at 10 dB below the peak vibration. Q_{10} ~ 3-10 have been reported to be measured from the basilar membrane of living animals in good physiological condition (Moore 1997; Pickles 1988; Robles and Ruggero 2001).
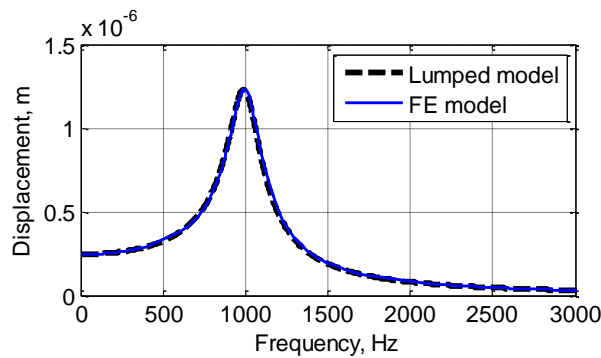

Fig. 4 The calculated frequency response from the analytical lumped element model compared to the simulated frequency response from the numerical finite element model of aluminium bridge gate B1 with l_b = 1.62 mm

As the bridge gate length decreases from B1 to B10, the resonant frequency has been simulated to increase to ~ 8 kHz while the displacement decreases to ~ 20 nm. Similarly, the basilar membrane in the cochlea has been measured by others to resonate with smaller amplitude displacements at higher frequencies, in which peak vibration of 20 nm is measured at 1 kHz while 2 nm is measured at 10 kHz (Moore 1997; Pickles 1988).

7

3.3.1 Lumped element model error

An increase of disagreement between the analytical lumped element model and numerical FE model has been observed as the bridge gate length decreases. The FE simulation results and lumped element model calculations for B7 - B10 of l_b = 0.81 mm - 0.57 mm are plotted together in Fig. 5a showing the increase of discrepancies between the two models as the bridge gate length decreases from B7 to B10. The resonant frequency from the FE model has been simulated to be higher than the lumped element model while the mechanical sensitivity is becoming smaller.
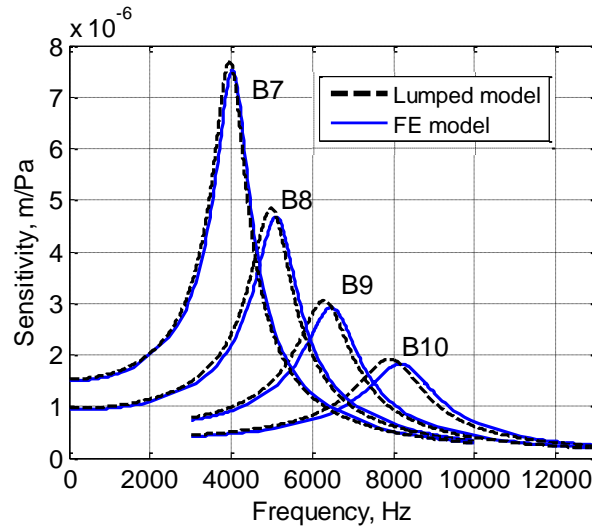
(a) Frequency responses for B7 - B10
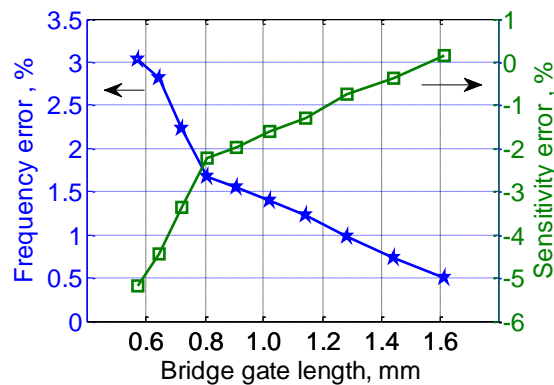
(b) FE and lumped element model percentage errors for B1 - B10
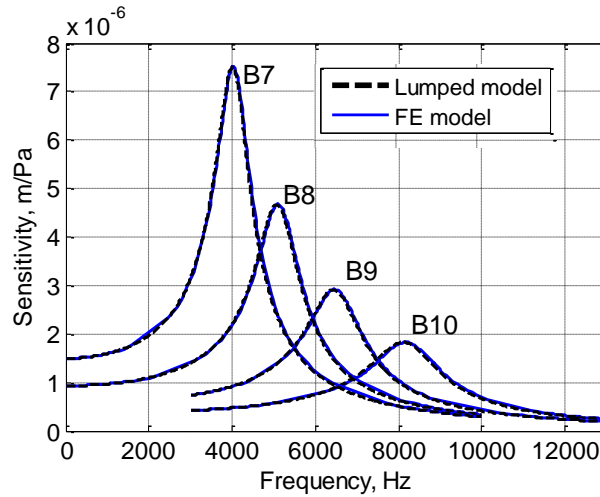
Fig. 5 a The comparison of frequency responses between FE model and lumped element model for aluminium bridge gate B7 - B10 of length l_b = 0.81 mm - 0.57 mm **b** The increase of frequency and mechanical sensitivity percentage errors between the FE and lumped element models as the bridge gate length decreases from B1 (l_b = 1.62 mm) to B10 (l_b = 0.57 mm). The positive(negative) percentage value indicates the resonant frequency or sensitivity of the FE model being higher(smaller) than lumped element model

The percentage differences between FE and lumped element model have been computed from the mechanical sensitivity and frequency of the aluminium bridge gates B1 - B10 i.e. l_b = 1.62 mm to 0.57 mm. Fig. 5b shows the frequency and sensitivity percentage difference between the two models. For B1 to B6 of l_b = 1.62 mm - 0.91 mm, the models agree well with each other, with the percentage errors for both frequency and sensitivity being less than 2 %. As the bridge gate length continues to decrease from B7 to B10, the percentage error for both frequency and sensitivity of the analytical lumped element model from the FE model have been calculated to increase more than 2 %. The discrepancies in frequency responses between the two models might be due to

8

the limitation of the analytical bridge gate theory, leading to inaccurate estimation of m, b and k for the lumped element model.

3.3.2 Lumped element model correction

In order to obtain a more accurate response of the bridge gate from the lumped element model, the approximate values of b and k parameters for the model can be extracted from the simulated response of the bridge gate in FE model. Thus, the lumped element model has been reconstructed using the estimated b and k from FE model plus the effective mass m of the bridge gate structure. The frequency responses from the reconstructed lumped element models have been calculated and fitted to the FE simulation results in Fig. 6a with small frequency and mechanical sensitivity percentage errors as shown in Fig. 6b.

(a) Frequency responses for B7 - B10
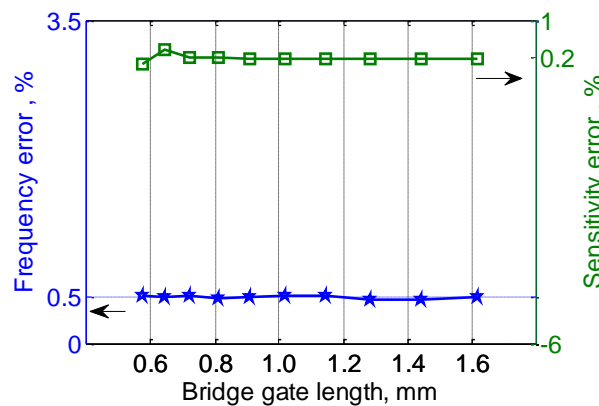
(b) FE and lumped element model percentage errors for B1 - B10

Fig. 6 The lumped element model has been reconstructed to fit the FE model. **a** The fitting of frequency responses from the reconstructed lumped element model to FE model for the aluminium bridge gates B7 - B10 of length l_b = 0.81 mm - 0.57 mm. **b** Small frequency and mechanical sensitivity percentage errors between the reconstructed lumped element and FE models as the bridge gate length decreases from B1 (l_b = 1.62 mm) to B10 (l_b = 0.57 mm)

In future, different shapes of MEMS resonator other than the simple form of bridge structure could be employed for better RGT cochlear model application, for instance the crab-legged or serpentine features. A complex theory and analysis will be required to design these complicated structures. In addition, advanced analysis is necessary in order to incorporate damping according to the structure's geometry and/or to account for the presence of different stress type, either compressive or tensile within the structures. Thus, FE model simulation

in *CoventorWare* can assist the analysis of the structure and better lumped element model can be developed from the corresponding FE model.

3.3.3 Lumped element model testing

The reconstructed analytical lumped element model for B1 has been tested with 0.01 Pa of noise input signal which represents the mechanical force F in Equ. (2). The noise input signal in analogue time domain is shown in Fig. 7a and the corresponding spectral domain representation of the input signal is plotted in Fig. 7b. The calculated mechanical response of the reconstructed analytical lumped element model for B1 is shown in Fig. 7c-d. B1 resonates at the designed frequency $f_1 \sim 1$ kHz and filters all other frequencies outside of the designed value. Next, the instantaneous vibration displacements of the bridge gate with respect to time, $x(t)$ in Fig. 7c will be transduced into the electrical signals within the channel region.
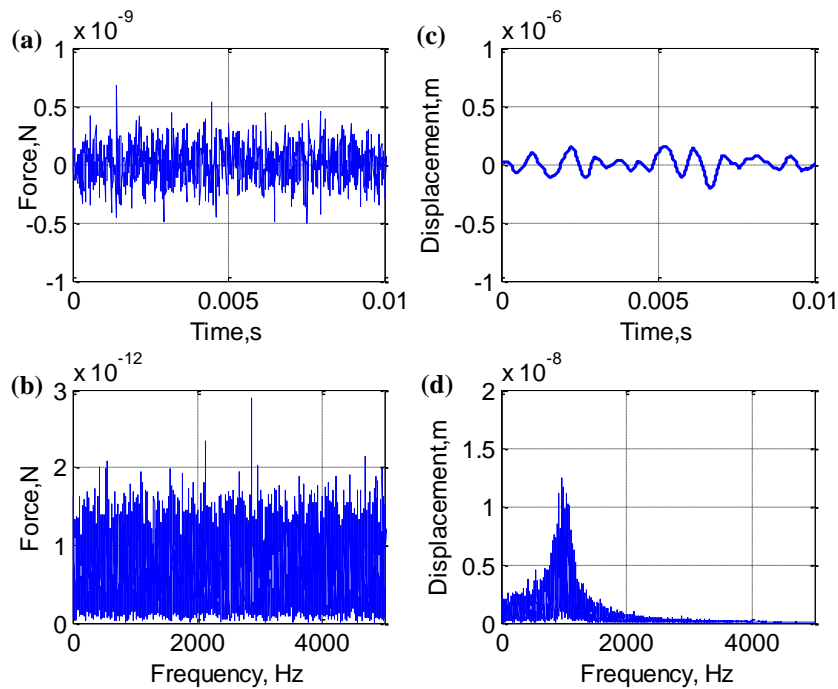

Fig. 7 The noise input signal in **a** time and **b** frequency domains. The calculated mechanical response of B1 in **c** time and **d** frequency domains with respect to the applied noise input

4 RGT electromechanical modelling

From Fig. 2, the cross sectional view of RGT device is shown in Fig. 8. Basically, the channel region consists of 1) the channel inversion layer within the silicon substrate and 2) the grown silicon dioxide layer as the gate oxide. The DC voltage V_{gs} is applied onto the bridge gate structure to modulate the channel conductance and V_{ds} is applied to induce the electrical current I_{ds} to flow from drain to source. The bridge gate instantaneous vibration $x(t)$ at the constant voltage V_{gs} will vary the modulation of channel conductance and thus vary the drain current I_{ds} with respect to time.

In this section, the electromechanical model of RGT device is presented. The RGT electrical sensitivity is defined as the change in current variation with respect to the change of sound input pressure applied on the aluminium bridge gate. From the model, the expected electrical sensitivity of RGT device operating in air has been estimated. The range of constant voltage V_{gs} that can be applied onto the bridge gate has been discussed, raising vital consideration on the limitation of the device operating region. The active characteristic of the RGT device due to the applied V_{gs} has been highlighted in this study.

10

4.1 Limit of V_{gs} for RGT

The pull-in voltage, V_{pi} is the maximum voltage that could be applied onto the bridge gate before the structure snapped/collapsed onto the channel region. The pull-in voltage is given by Equ. (8) where A_c is the area of channel region and ε_0 is the permittivity of air (Nathanson et al. 1967). From Fig. 8, the channel area is defined as $A_c = W_c \times L_c$ with W_c and L_c being the width and length of the channel. L_c also represents the width of the bridge gate, w_b. From the equation of bending, $k \propto \frac{1}{l_b^3}$ (Rebeiz 2003). Thus from Equ. (8), the pull-in voltage for B1 - B10 bridge gate structures will increase with respect to the decrease of l_b assuming t_b, w_b, E, d_i and A_c to be constant for each bridge gate.

$$V_{pi} = \sqrt{\frac{8k d_i^3}{27\varepsilon_0 A_c}} \qquad (8)$$

The regime of operation for V_{gs} is defined in Equ. (9). The pull-in voltage sets the maximum limit of the safe operating voltage or feedback control voltage that can be applied onto the bridge gate. Simultaneously, in order for the modulation of channel conductance to occur, the minimum DC bias applied onto the bridge gate needs to be higher than the threshold voltage V_{th} of the channel.
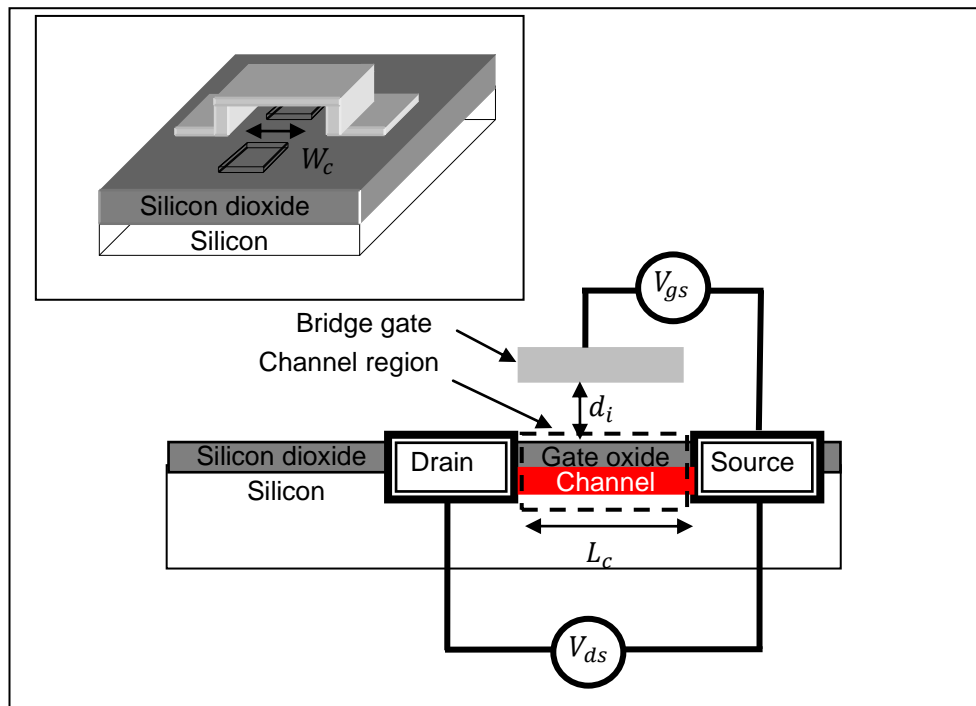
$$V_{th} < V_{gs} < V_{pi} \qquad (9)$$

Fig. 8 The cross sectional view of RGT device which is biased with V_{gs} and V_{ds} in order to induce current flow through the channel. d_i denotes the air gap distance from the channel region to bridge gate while L_c defines the channel length. In the subset, W_c defines the channel width

4.2 Electromechanical tuning of RGT

As the applied V_{gs} increases, there are 2 electromechanical effects to be expected to happen on the bridge gate structure. 1) The attractive electrostatic force between the bridge gate and channel increases. Thus, within the regime of operation for V_{gs}, the bridge gate undergoes a small deflection and the air gap distance reduces from

d_i to d_n without snapping onto the channel region as the applied V_{gs} increases. The relationship between the change in air gap spacing distance $(d_i - d_n)$ and the applied voltage onto the bridge gate V_{gs} is given by Equ. (10). 2) The interaction between electrostatic force and mechanical restoring force within the bridge gate causes the elastic restoring coefficient k to vary. In Equ. (11), k reduces to k_n with respect to the increase of V_{gs}. Consequently, the resonant frequency of the bridge gate is reduced from its designed mechanical resonant radial frequency of ω_o to ω_n as indicated in Equ. (12).

$$V_{gs} = \sqrt{\frac{2k(d_i - d_n)d_n^2}{\varepsilon_0 A_c}} \tag{10}$$

$$k_n = k - \frac{\varepsilon_0 A_c V_{gs}^2}{d_n^3} \tag{11}$$

$$\frac{\omega_n}{\omega_o} = \sqrt{\frac{k_n/m}{k/m}} \tag{12}$$

The analytical electromechanical response of RGT device that employs bridge gate B7 of length $l_b = 0.81$ mm has been investigated. From the lumped element model, the mechanical response of B7 without the influence of V_{gs} has been calculated and labelled as V_{gs0} in Fig. 9. The resonant frequency at V_{gs0} has been estimated to be $f_1 = 4$ kHz. The applied V_{gs} has been increased and the corresponding lumped element models based on the changes of k have been calculated. In our model, the tuning behaviour of the RGT device is calculated for $V_{gs1} = \frac{5V_{pi}}{10}$, $V_{gs2} = \frac{8V_{pi}}{10}$ and $V_{gs3} = \frac{9V_{pi}}{10}$, respectively. Fig. 9 demonstrates the tuning characteristics of B7 due to the applied voltages of $V_{gs1} < V_{gs2} < V_{gs3}$. With the increase of V_{gs0} to V_{gs3}, the resonant frequency decreases to 28 % from 4 kHz while the gain becomes ~2 times greater than the gain of the bridge gate at V_{gs0}. Thus, the amplitude of bridge gate vibration can be amplified or attenuated electrostatically by the applied DC voltage and at the same time, the tuning of resonant frequency can also be achieved. The active cochlea amplification characteristic is reproduced by having a non-zero V_{gs} component.
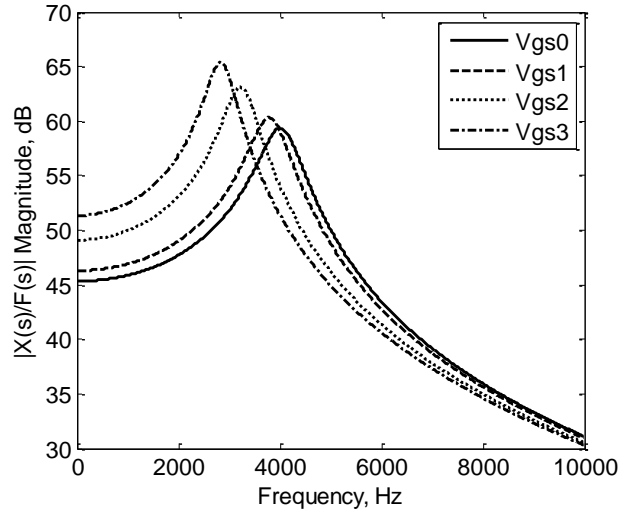

Fig. 9 The analytical lumped element model of B7 at different values of V_{gs} applied onto the bridge gate. At 0 V, $V_{gs} = V_{gs0}$ and then the applied voltage increases from V_{gs1} to V_{gs3}. The gain and resonant frequency of the bridge gate have been tuned electrostatically with respect to V_{gs}.

4.3 Capacitance model of RGT

In RGT, the part from the bridge gate to channel can be modelled as a parallel plate capacitor. The total capacitance between the bridge gate and channel per unit area C_{total} has been taken as the series capacitance of air C_{air} and gate oxide $C_{ox} = \frac{\varepsilon_{ox}}{t_{ox}}$. This is defined in Equ. (13) with ε_{ox} and t_{ox} being the permittivity and thickness of the silicon dioxide gate oxide layer. The DC biased bridge gate vibration, $x(t)$ induces capacitance variation with respect to time. Since $t_{ox} \ll d_n$, $C_{ox} \gg C_{air}(t)$ giving $C_{total}(t) \approx C_{air}(t)$.

$$C_{total}(t) = C_{air}(t) \parallel C_{ox} = \frac{\varepsilon_0}{d_n \mp x(t) + \frac{\varepsilon_0}{\varepsilon_{ox}} t_{ox}} \tag{13}$$

When the bridge gate experiences the electromechanical deflection, the air gap spacing is actually a function of position along the bridge gate. In this work, the analysis is further simplified by assuming that the effective value of air gap spacing distance d_n between the bridge gate and channel region to be independent of position.

4.4 Drain current I_{ds} response of RGT

The variation in total capacitance with respect to time $C_{total}(t)$ which is triggered by the vibration of bridge gate $x(t)$ held at a constant voltage V_{gs} is comparable to the operation of the MOSFET device in which the gate is fixed in position but the voltage applied onto the gate changes with respect to time $V_{gs}(t)$ (Nathanson et al. 1967). The drain current model for a MOSFET has been modified by including the effect of air gap spacing and electromechanical characteristics of the bridge gate, as described by $C_{total}(t)$ in Equ. (13). Thus, the drain current model for RGT in saturation regime is derived into Equ. (14) with μ being the mobility of the charge carriers within the channel.

$$I_{ds}(t) = \frac{\mu C_{total}(t)}{2} \frac{W_c}{L_c} \left(V_{gs} - V_{th} \right)^2 \tag{14}$$

Overall, V_{gs} can control both the magnitude of the bridge gate displacement $x(t)$ and the induced charges within the channel. Increasing the applied V_{gs} onto the bridge gate has been described in the previous section to reduce k and thus increases $x(t)$. At the same time, d_i is reduced to d_n giving higher $C_{total}(t)$ and smaller threshold voltage V_{th}. The total increment of $x(t)$, $C_{total}(t)$ and V_{gs} plus the reduction of V_{th} are expected to increase $I_{ds}(t)$. The transconductance g_m can be used to represent gain of the RGT device which quantifies the transduction of the bridge gate vibration $x(t)$ biased at a constant voltage V_{gs} into small signal drain current output $I_{ds}(t)$. By changing the role of the vibrating bridge gate structure at a constant voltage V_{gs} with the equivalent change in voltage $V_{gs}(t)$ applied on a fixed non-vibrating bridge gate, the transconductance g_m is defined in Equ. (15).

$$g_m = \frac{\partial I_{ds}(t)}{\partial V_{gs}(t)} = \mu C_{total} \frac{W_c}{L_c} \left(V_{gs} - V_{th} \right) \tag{15}$$

The drain current model for RGT with bridge gate B7 of length $l_b = 0.81$ mm has been created and tested with 0.01 Pa of noise input signal. The values of $W_c = 80$ μm, $L_c = 10$ μm, $t_{ox} = 55$ nm and $\mu = 1400$ cm²/Vs have been assumed in the model. The bridge gate voltage of $V_{gs1} = \frac{5V_{pi}}{10}$ has been considered and increased to $V_{gs2} = \frac{8V_{pi}}{10}$ and $V_{gs3} = \frac{9V_{pi}}{10}$. The applied bridge gate voltages are within the regime of operation for V_{gs} i.e. $V_{th} < V_{gs} < V_{pi}$ with the threshold voltage for B7 assumed to be $V_{th} = \frac{V_{pi}}{10}$. The RGT device operates within the saturation regime and the calculated electrical output drain current $I_{ds}(t)$ from the device at $V_{gs1} < V_{gs2} < V_{gs3}$

have been plotted in Fig. 10a. The amplitude of drain current in time domain has been seen to be amplified when the applied voltage onto the bridge gate increases.

In Fig. 10b, the calculated electrical sensitivities of RGT in spectral domain at $V_{gs1} < V_{gs2} < V_{gs3}$ are shown. The expected output currents at resonance for 1 Pa of input signal have been calculated to increase from ~ 2 μA to 18 μA with respect to the increase of V_{gs}. As the applied V_{gs1} increases to V_{gs3}, the gain of RGT increases to almost 8.5 times greater than the gain calculated at V_{gs1}, and the resonant frequency has decreased by 25 %. The tuning characteristics of I_{ds} at different values of V_{gs} have been observed to follow the electromechanical tuning characteristics of the bridge gate structure B7 from Fig. 9. This is similar to the electrical frequency response of one hair cell that has been reported to follow closely the mechanical frequency response of a section point in the basilar membrane (Moore 1997; Pickles 1988).
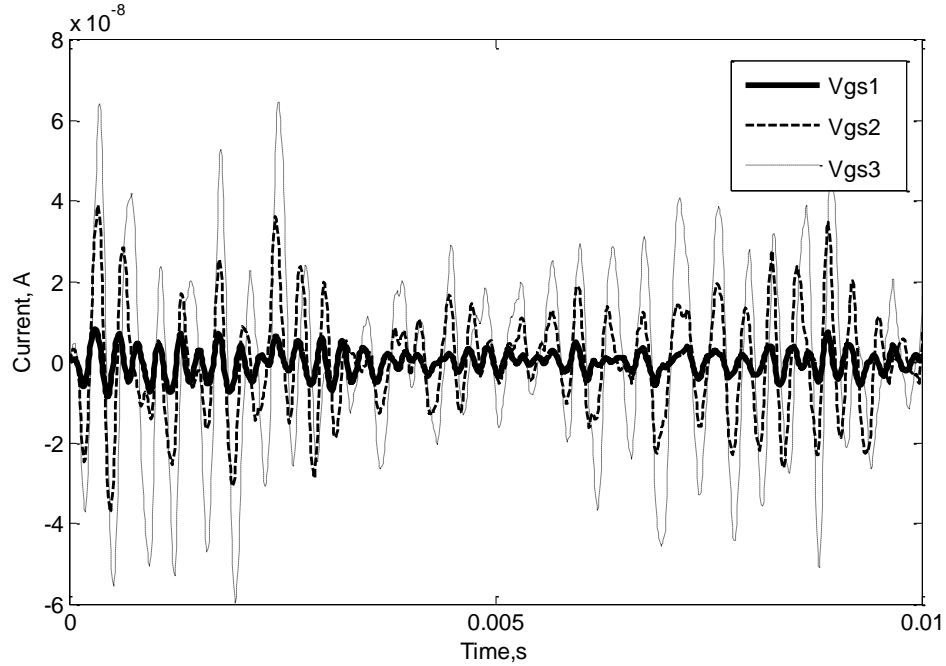
(a) I_{ds} in time domain
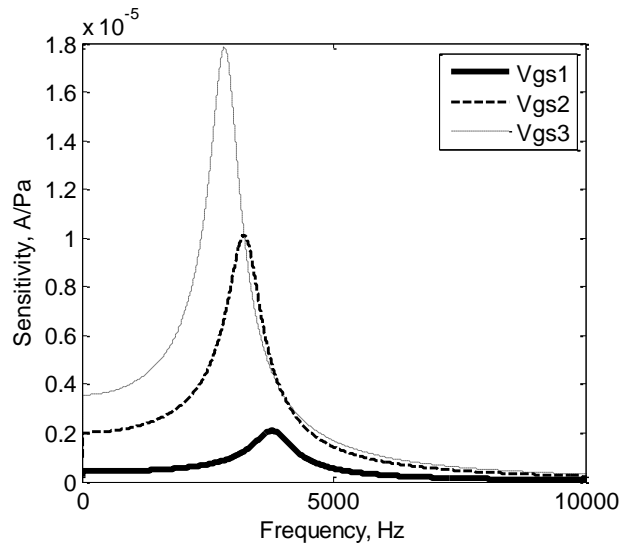
(b) Sensitivity of I_{ds} in frequency domain

Fig. 10 The calculated drain current response of RGT with B7 of $l_b = 0.81$ mm at $V_{gs1} < V_{gs2} < V_{gs3}$ **a** in time domain and **b** in frequency domain. The gain and resonant frequency of RGT have been tuned electrostatically with respect to V_{gs}.

14

5   RGT cochlear model fabrication design consideration

In this section, the established mathematical model for RGT has been used for fabrication design consideration and output estimation of the RGT cochlear model. The designed parameters for RGT have been optimised in order for the device to closely mimic the response of a human cochlear. The limitations in fabrication and the constraints in geometrical dimension of RGT have been discussed. The fabrication design for the threshold voltage and source/drain of RGT are not covered in this paper. The mask layout design for the fabrication of RGT cochlear model has been presented.

5.1 Influence of bridge gate width on quality factor

The material properties (E and ρ), length and thickness of the bridge gate have been fixed for the design of resonant frequency f_1. Table 2 shows the designed values of f_1 with respect to l_b. From Equ. (7), the remaining parameters that can be manipulated to design the quality factor Q_3 are the bridge gate width w_b, the distance between the bridge gate and substrate d_i and the viscosity of air ψ. Assuming $d_i = 4$ μm which is practical and feasible in fabrication, $\psi = 1.845\text{e}^{-5}$ kg/ms (Rebeiz 2003) and $w_b = 5$ μm, the quality factors of $Q_3 \sim 0.7 - 6$ have been estimated for the aluminium bridge gate with respect to $l_b = 1.62$ mm - 0.57 mm.

Table 2 The design of f_1 and Q_3 with respect to the geometrical dimensions (w_b, d_i and l_b) of the aluminium bridge gates.

Label	l_b , (mm)	f_1, kHz	w_b, μm	d_i , μm	Q_3
B1 - B10	1.62 - 0.57	1- 8	5	4	0.7-6

The lumped element models for aluminium bridge gates B1 - B10 have been created and the corresponding mechanical frequency responses have been calculated in order to estimate the quality factor Q_{10} which is measured at 10 dB below the peak vibration. Fig. 11 shows the frequency response of aluminium bridge gates B1 - B10 with a constant bridge gate width of 5 μm. As the bridge gate length decreases from B1 ($l_b = 1.62$ mm) to B10 ($l_b = 0.57$ mm), the quality factor has been estimated to increase from $Q_{10} \sim 0.4$ to $Q_{10} \sim 2$.
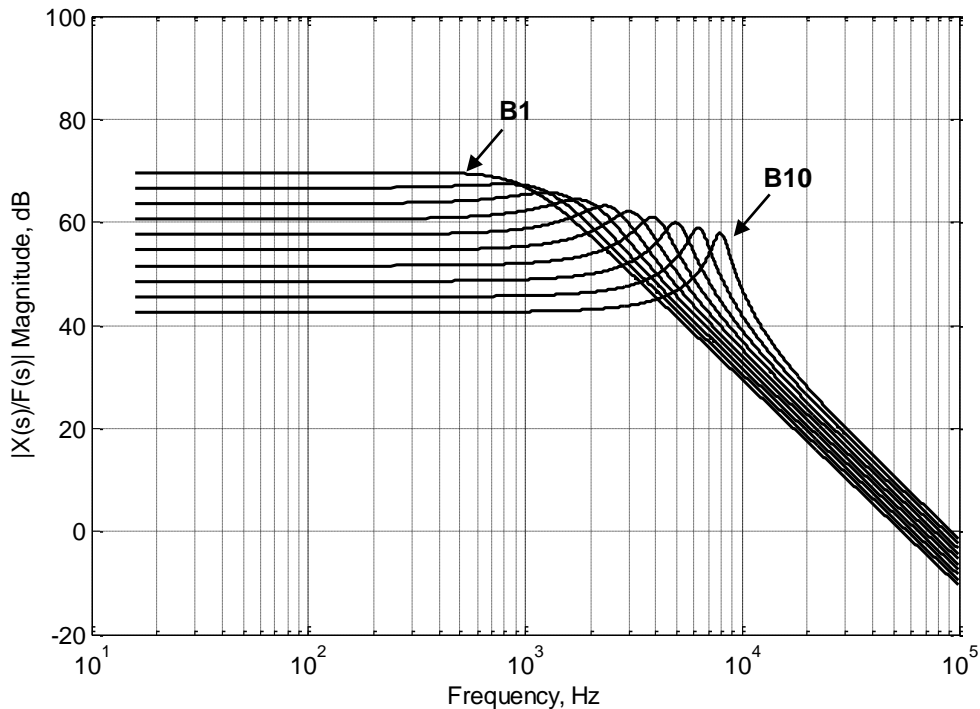

15

Fig. 11 The mechanical frequency response for aluminium bridge gates at a constant bridge gate width of $w_b = 5$. The quality factor has been estimated to increase from $Q_{10} \sim 0.4$ to 2 with respect to the decrease in bridge gate length from B1 ($l_b = 1.62$ mm) to B10 ($l_b = 0.57$ mm)

From the measured frequency response of a cochlea, the quality factor is approximately constant at each resonant frequency point f_1. The quality factor of the bridge gate can then be optimised by changing the distance of the bridge gate to the substrate or controlling the viscosity of surrounding medium, but these actions will affect all bridge gates in the array. In order to have individual control of the damping for each bridge gate, different width w_b can be assigned for each bridge gate length. High(low) quality factor can be reduced(increased) by fabricating wider(narrower) bridge gates and thus, bigger(smaller) air squeeze film damping effect could be attained (Haronian and MacDonald 1995). A constant quality factor of $Q_{10} \sim 2$ for each aluminium bridge gate can be achieved by varying the bridge gate width from $w_b = 2$ µm for B1 ($l_b = 1.62$ mm) to $w_b = 5$ µm for B10 ($l_b = 0.57$ mm), as shown in Fig. 12.

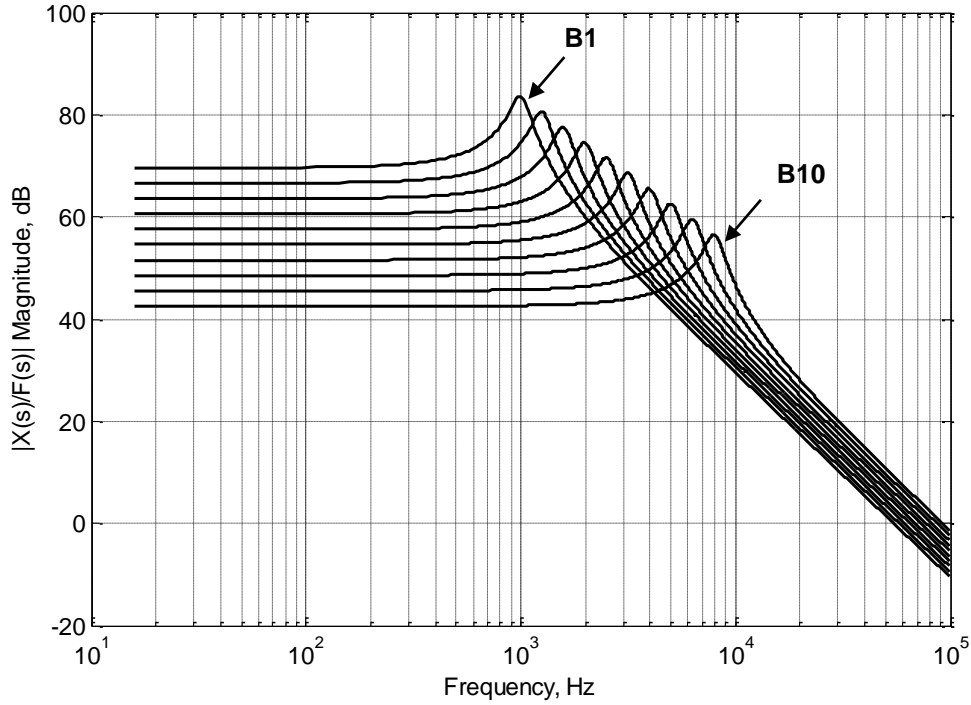**Fig. 12** The mechanical frequency response for aluminium bridge gates with the increase of bridge gate width from $w_b = 2$ µm to $w_b = 5$ µm with respect to the decrease in length from $l_b = 1.62$ mm (B1) to 0.57 mm (B10). The quality factor has been estimated to be constant at $Q_{10} \sim 2$.

5.2 Channel design

The geometrical dimensions of bridge gate (w_b, t_b, d_i and l_b) have been designed to copy the mechanical response of cochlea (f_1 and Q_{10}). The design for channel region of RGT is limited as the channel length L_c is set by the bridge gate width w_b and the distance from the channel to bridge gate is given by d_i. Channel width W_c is the only parameter left that can be manipulated to design the pull-in voltage and transconductance of RGT.

$$V_{pi} = \sqrt{\frac{4.74 E t_b^{\,3} d_i^{\,3}}{\varepsilon_0 W_c l_b^{\,3}}} \tag{16}$$

The equation for pull-in voltage V_{pi} is simplified from Equ. (8) to Equ. (16). The pull-in voltage will decrease with respect to the increase of bridge gate length l_b. Thus, different bridge gate length requires different regime

16

of operation for V_{gs} which has been defined previously as $V_{th} < V_{gs} < V_{pi}$. It is clear that longer bridge gate with smaller V_{pi} needs to operate at smaller regime of operation for V_{gs} in order to avoid the pull-in condition. Problem arises if the pull-in voltage V_{pi} is smaller than the threshold voltage V_{th}. The decrease in size of W_c will help to increase the pull-in voltage for the bridge gate but at the same time will also reduce the transconductance g_m of RGT as shown by Equ. (15). Thus, the optimisation of W_c needs to compromise between V_{pi} and g_m. A depletion mode channel instead of enhancement can be employed to solve this problem as the channel is always 'on' and thus satisfies the required $V_{th} < V_{gs} < V_{pi}$ regime of operation (Nathanson et al. 1967).

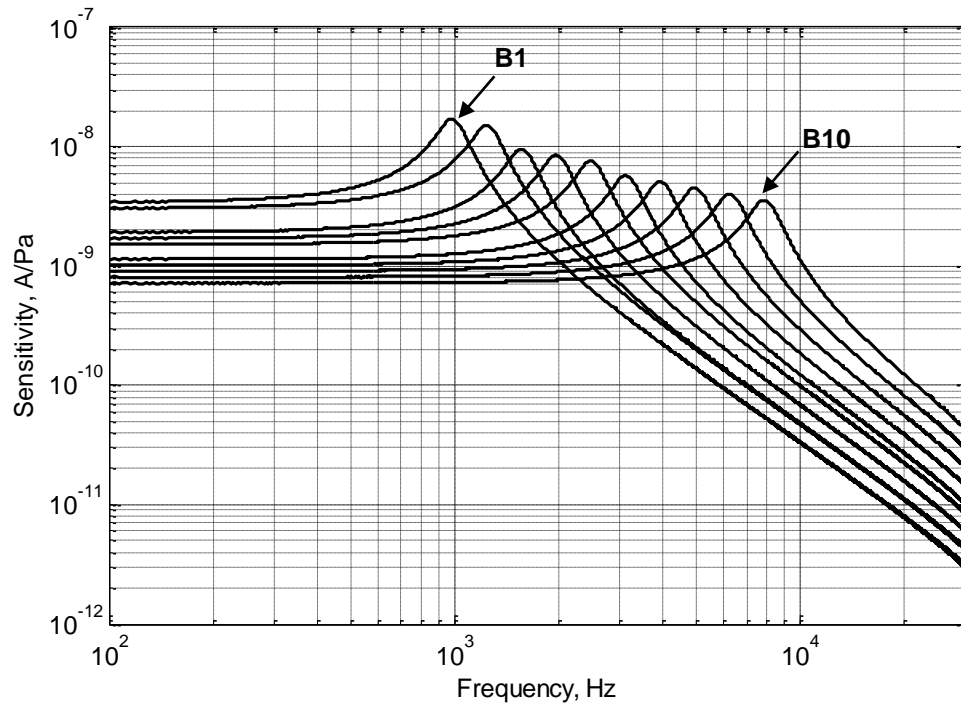## 5.3 Mechanical and electrical sensitivity of RGT cochlear model

The mechanical and electrical sensitivity of RGT cochlear model have been estimated using the optimised geometrical dimensions for the aluminium bridge gates B1 - B10, assuming $W_c = 5$ μm and $V_{th} = \frac{V_{pi}}{10}$ for the channels. At $V_{gs} = \frac{V_{pi}}{5}$, the sensitivities have been estimated from the RGTs and plotted in Fig. 13. In Fig. 13a, the mechanical sensitivity has decreased from ~ 100 μm/Pa to ~ 2 μm/Pa with respect to the decrease in bridge gate length from $l_b = 1.62$ mm (B1) to 0.57 mm (B10) while for the electrical sensitivity, the value has decreased from ~ 17 nA/Pa to ~ 4 nA/Pa, as shown in Fig. 13b. Taking into account the distance of $d_i = 4$ μm from the bridge gate to substrate, the sound input signal of smaller than 1 Pa should be applied in order to obtain nanometer range of vibration displacements from the bridge gates. The live cochlea possesses mechanical sensitivity of approximately 10 μm/Pa to 15 μm/Pa, while other developed cochlear models have been reported to provide responses of four to five orders of magnitude less (Bell 2006). Our proposed RGT cochlear model design in this paper suggests better sensitivity.

5.4 Layout design

The layout design for two arrays of RGTs which employ the bridge gates B1 - B10 on a single chip of size 1 cm × 1 cm is shown in Fig. 14. The channel region and source/drain have been assigned for each bridge gate structure. The channels have been positioned underneath the expected fundamental antinode location of the bridge gate vibration. At this position, the vibration displacement is at maximum level i.e. peak amplitude. Thus, maximal transduction from the mechanical structure to the channel region can be achieved. In order to obtain individual control of the RGT devices, different drive and sense circuitry have been designed to connect each bridge gate, source and drain to the bond pads.
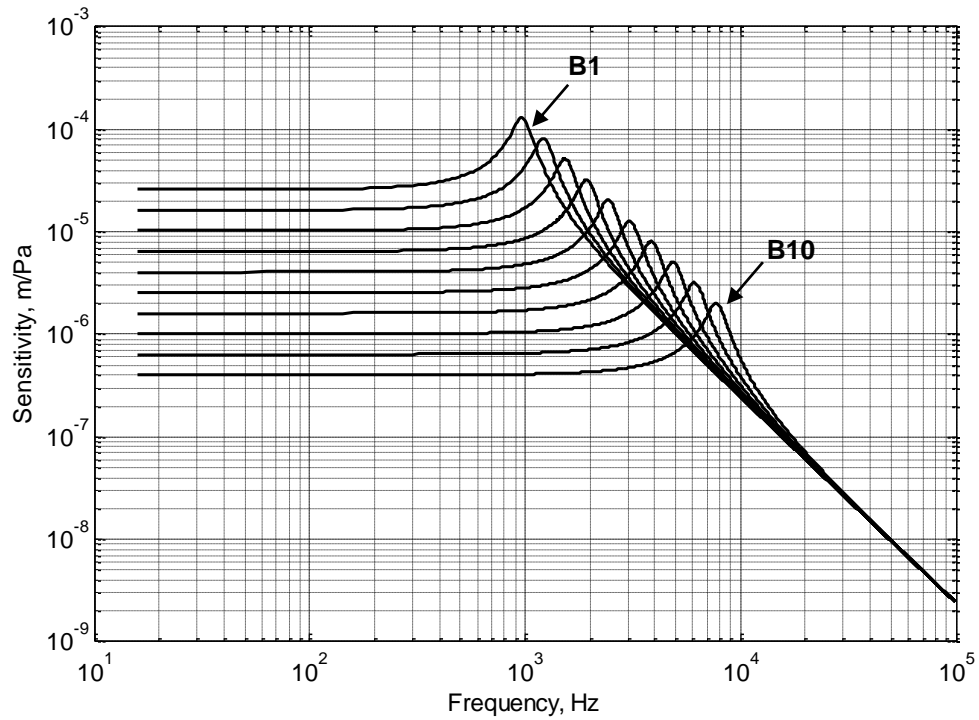
(a) Mechanical sensitivity

(b) Electrical sensitivity

Fig. 13 The calculated sensitivities for RGTs with aluminium bridge gates B1 - B10. **a** The mechanical sensitivities of ~ 100 μm/Pa - 2 μm/Pa and **b** the electrical sensitivities of ~17 nA/Pa - 4 nA/Pa have been estimated with respect to the decrease in bridge gate length from $l_b = 1.62$ mm (B1) to 0.57 mm (B10)
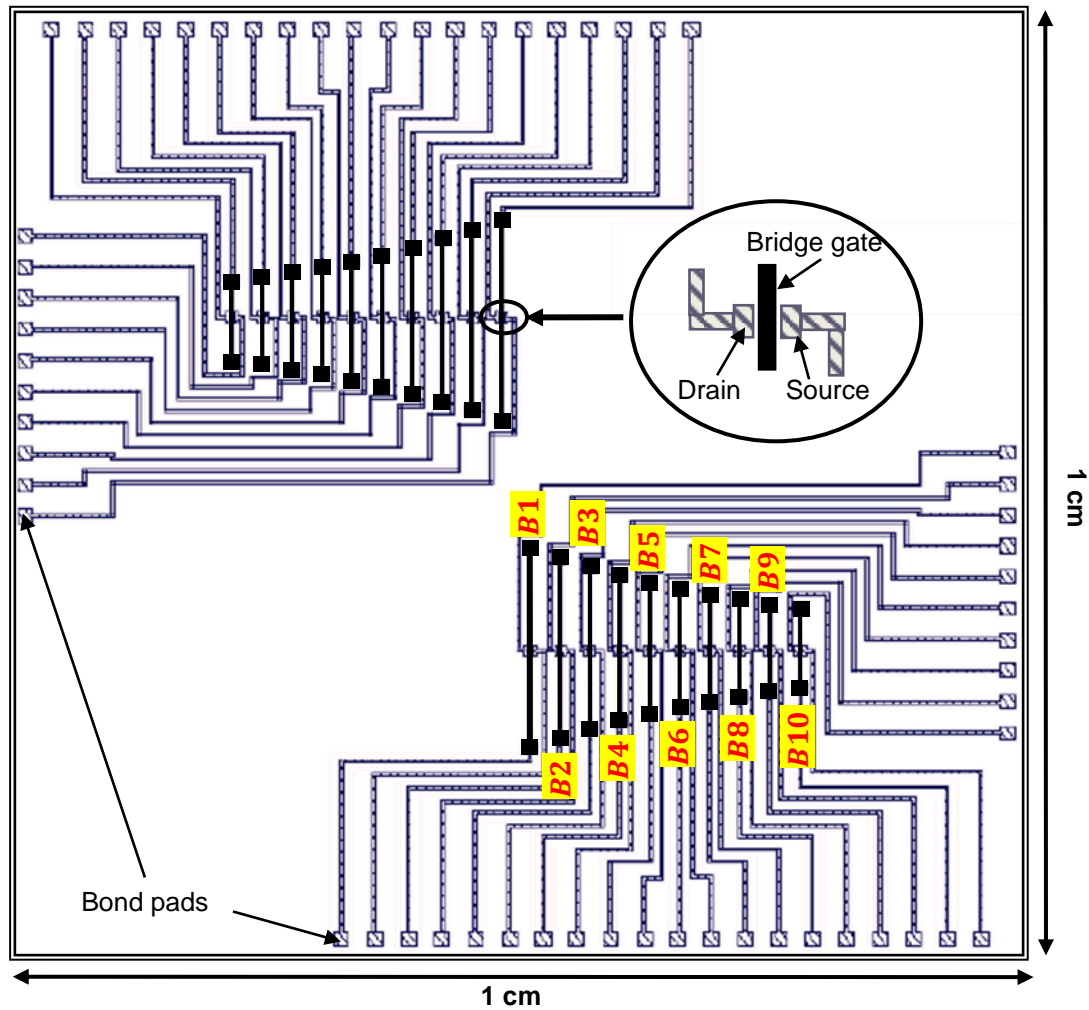
Fig. 14 The layout design (top view) for two arrays of RGTs on 1 cm × 1 cm of chip size, including the drive and sense circuitry that connect each bridge gate, source and drain to the bond pads. Bridge gates B1 - B10 of length l_b = 1.62 mm - 0.57 mm are employed for the RGT devices

6   Conclusions

Detailed mathematical modelling and new design analysis of RGT in order to mimic closely the mechanical and electrical frequency responses of the human cochlear have been presented. Small discrepancies between the analytical lumped element model and numerical finite element model of the bridge gate structures have been discussed. The lumped element model of the bridge gate has been introduced into the modified drain current model of the MOSFET. From the developed model, reasonable mechanical and electrical sensitivities of the RGTs have been estimated for the RGT cochlear model. The adaptive ability of RGT has been demonstrated by the self-tuning of sensitivity and selectivity with respect to the voltage applied onto the bridge gate, V_{gs}. The increase of V_{gs} has been found to amplify the gain of RGT and reduce the resonant frequency. For safe working operation of RGT, the regime of operation for V_{gs} has been deduced to be smaller than the pull-in voltage and bigger than the threshold voltage. The material properties and geometrical design of RGT has been found to be the crucial aspects in attaining the cochlear-like responses and characteristics. The bridge gate width plays an important role for determining the quality factor of the mechanical response while the channel width compromises the design for pull-in voltage and transconductance of RGT. Overall, a physiologically plausible physical model of the active human cochlear has been presented, imitating several known features of the cochlea.

References

Abelé N, Pott V, Boucart K, Casset F, Séguéni K, Ancey P, Ionescu AM (2005) Comparison of RSG-MOSFET and capacitive MEMS resonator detection. Electron Lett 41:242-244

Bachman M, Zeng F, Xu T, Li GP (2006) Micromechanical resonator array for an implantable bionic ear. Audiol Neuro-Otol 2:95-103

Bell A (2006) Sensors, motors, and tuning in the cochlea: interacting cells could form a surface acoustic wave resonator. Bioinspir Biomim 1:96-101

Elliott SJ, Shera CA (2012) The cochlea as a smart structure. Smart Mater Struct 21:064001

Hall NA, Okandan M, Littrell R, Bichen B, Degertekin FL (2008) Simulation of thin-film damping and thermal mechanical noise spectra for advanced micromachined microphone structures. J Microelectromech S 17:688-697

Han SM, Benaroy H, Wei T (1999) Dynamics of transversely vibrating beams using four engineering theories. J Sound Vib 225:935-988

Haronian D, MacDonald NC (1995) A microelectromechanics based artificial cochlear (MEMBAC). In: International Conference on Solid-State Sensors and Actuators, and Eurosensors IX, pp 708-711

Koickal TJ et al. (2011) Design of a spike event coded RGT microphone for neuromorphic auditory systems. In: IEEE International Symposium on Circuits and Systems (ISCAS) pp 2465-2468

Latif R (2012) Microelectromechanical systems for biomimetical application. Ph.D Thesis, The University of Edinburgh

Latif R et al. (2010) Microelectromechanical systems for biomimetical applications. J Vac Sci Technol B 28:C6N1-C6N6

Latif R et al. (2011) Low frequency tantalum electromechanical systems for biomimetical applications. J Vac Sci Technol B 29:06FE05

Latif R, Sanei S, Nazarpour K (2008) Classification of elbow electromyography signals based on directed transfer functions. In: International Conference on BioMedical Engineering and Informatics, pp 371-374

Li P, Fang Y (2009) A new free molecular model for squeeze film damping of flexible microbeam in low vacuum. Micro and Nanosystems 1:68-71

Liu C (2007) Micromachined biomimetic artificial haircell sensors. Bioinspir Biomim 2:S167-S169

Liwei S, Guo S, Asaka K (2010) A novel jellyfish-like biomimetic microrobot. In: IEEE/ICME International Conference on Complex Medical Engineering (CME), pp 277-281

Mastropaolo E, Latif R, Grady E, Cheung R (2013) Control of stress in tantalum thin films for the fabrication of 3D MEMS structures. J Vac Sci Technol B 31:06FD02

Mastropaolo E, Latif R, Koickal T, Hamilton A, Cheung R, Newton M, Smith L (2012) Bimaterial electromechanical systems for a biomimetical acoustic sensor. J Vac Sci Technol B 30:06FD01

Moore BCJ (1997) An Introduction to the Psychology of Hearing. Academic Press Limited, London

Nathanson HC, Newell WE (1965) A resonant-gate silicon surface transistor with high-Q band-pass properties. Appl Phys Lett 7:84-86

Nathanson HC, Newell WE, Wickstrom RA, Davis JR (1967) The resonant gate transistor. IEE Transaction of Electronic Device 14:117-133

Pickles JO (1988) An Introduction to the Physiology of Hearing vol 81. Academic Press Limited, London

Rebeiz GM (2003) RF MEMS theory, design, and technology. John Wiley & Sons, New Jersey

Robles L, Ruggero MA (2001) Mechanics of the mammalian cochlea. Physiology Reviews 81:1305-1352

Striemer CC, Gaborski TR, McGrath JL, Fauchet PM (2007) Charge- and size-based separation of macromolecules using ultrathin silicon membranes. Nature 445:749-753

Wang S et al. (2012) A low-noise interface circuit for MEMS cochlea-mimicking acoustic sensors. In: IEEE International Symposium on Circuits and Systems (ISCAS), pp 1151-1154

White RD, Grosh K (2002) Design and characterisation of MEMS piezoresistive cochlear-like acoustic sensor. In: Proceedings of the 2002 ASME International Mechanical Engineering Congress and Exposition, pp 201-210

White RD, Grosh K (2005) Microengineered hydromechanical cochlear model. In: P Natl Acad Sci Usa, pp 1296-1301